MULTIGAP SIGNATURES IN THE SUPERFLUID RESPONSE OF IRON-BASED SUPERCONDUCTORS

O.K. GANIEV[1,2,3,4,a], Z.I. RAKHMONOV[5]

[1]New Uzbekistan University, Movarounnahr Str., 1, 100000 Tashkent, Uzbekistan
[2]Central Asian University, 264, Milliy bog Str., 111221 Tashkent, Uzbekistan
[3]Institute of Nuclear Physics, AS RUz, 100214 Tashkent, Uzbekistan
[4]National University of Uzbekistan, 100174 Tashkent, Uzbekistan
Corresponding author[a]: oganiev@yahoo.com
[5]Engineering Physics Institute, Samarkand State University, 140104 Samarkand, Uzbekistan

Received May 7, 2025

Abstract. A theoretical investigation of two-gap superconductivity in iron-based superconductors is presented, using a self-consistent two-band model. This model is necessitated by the presence of two distinct superconducting energy gaps in these materials. The temperature dependence of the superfluid density (ρ_s), London penetration depth (λ_L), and lower critical magnetic field (H_{c1}) are calculated within this framework. Comparative analysis demonstrates that the two-band model provides a significantly improved description of these properties compared to a single-band BCS model. Furthermore, the individual energy gaps exhibit distinct temperature dependencies, and the contributions to the overall superfluid density from each electronic band are shown to be qualitatively different. The theoretical predictions are found to be in good quantitative agreement with available experimental data, thus validating the two-band model and emphasizing the crucial role of multi-band physics in the superconducting state of iron-pnictides.

Key words: Two-band model, superfluid density, London penetration depth, lower critical field, iron-based superconductors.

DOI: https://doi.org/10.59277/RomJPhys.2025.70.619

1. INTRODUCTION

The discovery of iron-based superconductors (FeSCs) in 2008 [1] generated significant interest in the condensed matter physics community. These materials offered a new platform for exploring unconventional superconductivity, departing from the conventional Bardeen-Cooper-Schrieffer (BCS) theory [2] that successfully describes many conventional superconductors. Unlike BCS superconductors, where electron pairing is mediated by phonons, FeSCs exhibit a complex interplay of electronic phases and potentially novel pairing mechanisms, which remain under active investigation [3]. This "unconventional" nature often involves non-phonon-mediated pairing (such as spin fluctuations), higher angular momentum pairing symmetries (beyond s-wave), and a close proximity to other ordered states, notably antiferromagnetism.

Crucial parameters for understanding the superconducting state in FeSCs are the superfluid density (ρ_s), the London penetration depth (λ_L), and the lower critical

magnetic field (H_{c1}). The superfluid density, ρ_s, reflects the density of superconducting charge carriers and the rigidity of the superconducting condensate [4], while λ_L is the characteristic length scale over which an external magnetic field is screened within the superconductor. The lower critical field, H_{c1}, marks the onset of magnetic flux penetration into a type-II superconductor, providing information about the thermodynamic stability of the superconducting state. In FeSCs, ρ_s (and thus λ_L, since $\rho_s \propto \lambda_L^{-2}$) is frequently determined experimentally using techniques like muon spin relaxation (μSR) [5, 6]. The lower critical field, H_{c1}, is typically measured using magnetization or specific heat and angle-resolved photoemission spectroscopy (ARPES) measurements [7–10].

Experimental measurements reveal a diverse range of behaviors for $\rho_s(T)$, $\lambda_L(T)$, and $H_{c1}(T)$ across different FeSC families (such as the 1111, 122, 11, and 111 systems). Some materials display the characteristic saturation of ρ_s and λ_L^{-2} at low temperatures, and a $(1-T/T_c)^{1/2}$ dependence of H_{c1} near T_c, all expected for a fully gapped s-wave superconductor. Others, however, exhibit power-law dependencies of $\rho_s(T)$ (and correspondingly, $\lambda_L(T)$) at low temperatures, and deviations from the simple square-root dependence in $H_{c1}(T)$, indicating the presence of "nodal points" in the superconducting energy gap [11]. These nodes, points on the Fermi surface where the energy gap vanishes, signify non-traditional pairing symmetries, such as d-wave or $s^{\pm}$ [12], and they break the full-gap protection against quasiparticle excitations, leading to the observed power-law behavior. The absolute values of ρ_s, λ_L, and H_{c1}, and their evolution with doping, provides further insight into the strength of electronic correlations and the contributions of different regions of the Fermi surface to the pairing [13].

A key feature observed in many FeSC families is the "two-gap" behavior, manifesting in $\rho_s(T)$, $\lambda_L(T)$, and $H_{c1}(T)$ [14–16]. This is characterized by distinct changes in the slope of these quantities at different temperature ranges, suggesting the presence of two distinct superconducting energy gaps. This multi-gap behavior is directly related to the electronic structure of FeSCs, which typically possess multiple Fermi surface sheets – both electron and hole pockets. Different superconducting gaps can open on these different Fermi surface sheets, leading to the observed two-gap phenomenology.

To interpret this two-gap behavior, the phenomenological α-model [13, 17–22] is often employed. This model extends the single-band BCS theory by assuming two independent s-wave gaps, Δ_1 and Δ_2, with weighting factors α_1 and α_2 (where $\alpha_1 + \alpha_2 = 1$). The superfluid density is then calculated as a weighted average of the BCS-like contributions from each gap: $\rho_s(T) = \alpha_1 \rho_{s,BCS}(T, \Delta_1) + \alpha_2 \rho_{s,BCS}(T, \Delta_2)$. The α parameters represent the relative contributions of each band to the overall superfluid density. Similar expressions can be derived for $\lambda_L(T)$ and, in principle, for $H_{c1}(T)$, although the latter is more complex. While the α-model can successfully

fit experimental data for many FeSCs, its fundamental assumption of zero interband coupling is problematic. Zero coupling would imply independent superconducting transitions for each band, contradicting the observation of a single critical temperature (T_c) in these materials.

This limitation motivates the use of more sophisticated theoretical approaches, particularly the self-consistent two-gap model [23–27]. This model explicitly incorporates "interband" pairing interactions, in addition to intraband interactions. Specifically, the model considers intraband pairing interactions (V_{11}, V_{22}) within each band and interband pairing interactions (V_{12}, V_{21}) between the bands. The two gaps, Δ_1 and Δ_2, are then determined self-consistently by solving a set of coupled gap equations that depend on all these interaction parameters. Crucially, the interband coupling (V_{12}, V_{21}) is responsible for the emergence of a single T_c, even in the presence of different gap magnitudes on different Fermi surface sheets. This model allows for a more accurate calculation of $\rho_s(T)$, $\lambda_L(T)$, and $H_{c1}(T)$ in the two-gap scenario.

In this paper, we delve into the theoretical underpinnings of the two-gap behavior observed in the superfluid density, penetration depth, and lower critical field of FeSCs. We present the self-consistent two-gap model as a more physically realistic framework for describing multi-gap superconductivity in these materials. We investigate the influence of the two-gap structure on the temperature dependencies of ρ_s, λ_L, and H_{c1}, particularly in materials exhibiting clear two-gap characteristics. This analysis will deepen our understanding of the interplay between superconductivity and other electronic properties in FeSCs, including the normal state resistivity (which often exhibits non-Fermi liquid behavior), the proximity to antiferromagnetic order (which is often suppressed by doping to induce superconductivity), and any potential structural transitions that might correlate with the superconducting state. The insights gained from this theoretical study will be directly compared with experimental data, providing a comprehensive picture of two-gap superconductivity in iron-based materials.

2. SELF-CONSISTENT TWO-GAP APPROACH

Shortly after the development of the BCS theory, Suhl *et al.* [28] and Moskalenko [29] proposed a self-consistent two-gap model to describe superconductors with a more complex Fermi surface topology than those described by the weakly-coupled BCS theory. This model was soon extended [30] by incorporating an interband scattering potential for Cooper pairs – an important addition, which enhances pair scattering *via* an additional exchange channel. Kogan *et al.* [16, 27] and Bussmann-Holder *et al.* [23, 25] revisited this two-gap model, focusing on isotropic s-wave gaps.

Within the two-gap approach, the temperature dependence of the two gaps (Δ_1

and Δ_2) is obtained from a self-consistent set of coupled gap equations, as follows:

$$\begin{aligned}
\Delta_1 &= \int_0^{\omega_{D1}} \frac{N_1(0)V_{11}\Delta_1}{\sqrt{\varepsilon^2+\Delta_1^2}} \tanh\left(\frac{\sqrt{\varepsilon^2+\Delta_1^2}}{2k_BT}\right) d\varepsilon \\
&\quad + \int_0^{\omega_{D2}} \frac{N_2(0)V_{12}\Delta_2}{\sqrt{\varepsilon^2+\Delta_2^2}} \tanh\left(\frac{\sqrt{\varepsilon^2+\Delta_2^2}}{2k_BT}\right) d\varepsilon \\
\Delta_2 &= \int_0^{\omega_{D1}} \frac{N_1(0)V_{21}\Delta_1}{\sqrt{\varepsilon^2+\Delta_1^2}} \tanh\left(\frac{\sqrt{\varepsilon^2+\Delta_1^2}}{2k_BT}\right) d\varepsilon \\
&\quad + \int_0^{\omega_{D2}} \frac{N_2(0)V_{22}\Delta_2}{\sqrt{\varepsilon^2+\Delta_2^2}} \tanh\left(\frac{\sqrt{\varepsilon^2+\Delta_2^2}}{2k_BT}\right) d\varepsilon. \qquad (1)
\end{aligned}$$

Here, $N_1(0)$ and $N_2(0)$ are the partial densities of states for each band at the Fermi level. V_{11} (V_{22}) and V_{12} (V_{21}) are the intraband and interband interaction potentials, respectively. ω_{D1} (ω_{D2}) is the Debye (cutoff) phonon frequency for band 1 (2).

Simplification of the above expressions can be achieved using the notation for the coupling constant $\lambda_{ij} = N_j(0)V_{ij}$. Further simplification is attained by assuming the same Debye frequency for both bands, *i.e.* $\omega_{D1} = \omega_{D2} = \omega_D$. The gap equations then become:

$$\begin{aligned}
\Delta_1 &= \int_0^{\omega_D} \frac{\lambda_{11}\Delta_1}{\sqrt{\varepsilon^2+\Delta_1^2}} \tanh\left(\frac{\sqrt{\varepsilon^2+\Delta_1^2}}{2k_BT}\right) d\varepsilon \\
&\quad + \int_0^{\omega_D} \frac{\lambda_{12}\Delta_2}{\sqrt{\varepsilon^2+\Delta_2^2}} \tanh\left(\frac{\sqrt{\varepsilon^2+\Delta_2^2}}{2k_BT}\right) d\varepsilon \\
\Delta_2 &= \int_0^{\omega_D} \frac{\lambda_{21}\Delta_1}{\sqrt{\varepsilon^2+\Delta_1^2}} \tanh\left(\frac{\sqrt{\varepsilon^2+\Delta_1^2}}{2k_BT}\right) d\varepsilon \\
&\quad + \int_0^{\omega_D} \frac{\lambda_{22}\Delta_2}{\sqrt{\varepsilon^2+\Delta_2^2}} \tanh\left(\frac{\sqrt{\varepsilon^2+\Delta_2^2}}{2k_BT}\right) d\varepsilon. \qquad (2)
\end{aligned}$$

The superconducting transition temperature is given by the expression

$$T_c = \left(\frac{2\omega_D e^{\gamma_E}}{\pi}\right) e^{-\frac{1}{\lambda}}, \qquad (3)$$

where γ_E is Euler's constant, and λ is the largest eigenvalue of the matrix λ_{ij}:

$$\lambda = \frac{\lambda_{11}+\lambda_{22}}{2} + \sqrt{\frac{(\lambda_{11}-\lambda_{22})^2}{4} + \lambda_{12}\lambda_{21}}. \tag{4}$$

Furthermore, within the framework of the isotropic s-wave superconducting gap scenario, the temperature dependence of the normalized superfluid density $\rho_s(T)/\rho_s(0)$ can be obtained analytically:

$$\frac{\rho_s(T)}{\rho_s(0)} = 1 - \frac{1}{2k_BT}\int_0^\infty \cosh^{-2}\left[\frac{\sqrt{\varepsilon^2+\Delta(T)^2}}{2k_BT}\right] d\varepsilon. \tag{5}$$

However, for materials exhibiting multi-gap behavior, such as many FeSCs, this single-band description is insufficient. Within the framework of the two-gap scenario, the normalized total superfluid density $\rho_s(T)/\rho_s(0)$, is a weighted sum of the contributions from each band:

$$\frac{\rho_s(T)}{\rho_s(0)} = \frac{\rho_{s1}(T)+\rho_{s2}(T)}{\rho_s(0)} = w_\rho \frac{\rho_{s1}(T)}{\rho_{s1}(0)} + (1-w_\rho)\frac{\rho_{s2}(T)}{\rho_{s2}(0}, \tag{6}$$

where the indices 1 and 2 refer to the two bands (and their associated gaps Δ_1 and Δ_2), $\rho_s(0) = \rho_{s1}(0) + \rho_{s2}(0)$ is the total zero-temperature superfluid density, and $\rho_{sj}(T)/\rho_{sj}(0)$ is calculated using equation (5) with the respective gap $\Delta_j(T)$. The weighting factor w_ρ represents the fractional contribution of the first band (associated with gap Δ_1) to $\rho_s(0)$. It is physically related to the ratio electronic properties of the bands, such as $w_\rho = \Delta_1/\Delta_2$.

In the superconducting state, the material exhibits the Meissner effect, expelling magnetic fields below a threshold value known as the lower critical magnetic field $H_{c1}(T)$. Above $H_{c1}(T)$, it becomes energetically favorable for magnetic flux to penetrate the superconductor in the form of quantized flux vortices. This lower critical field is related to the fundamental properties of the superconductor:

$$H_{c1}(T) = \frac{\Phi_0}{4\pi\mu_0\lambda_L^2(T)}(\ln\kappa(T)+0.5), \tag{7}$$

where $\Phi_0 = h/2e$ is the magnetic flux quantum, μ_0 is the permeability of free space, and $\lambda_L(T)$ is the London penetration depth. The term $(\ln\kappa(T)+0.5)$ approximates the vortex line energy and is valid in the limit of large Ginzburg-Landau parameter $\kappa >> 1$, a regime commonly applicable to type-II superconductors like FeSCs. The Ginzburg-Landau parameter itself is defined as $\kappa(T) = \lambda_L(T)/\xi(T)$, the ratio of the magnetic penetration depth to the superconducting coherence length. Equation (7) highlights the strong dependence of $H_{c1}(T))$ on $\lambda_L(T)$.

The London penetration depth $\lambda_L(T)$, characterizes the length scale over which an external magnetic field is screened inside the superconductor. It is fundamentally

linked to the superfluid density:

$$\lambda_L(T) = \sqrt{\frac{m^*}{\mu_0 \rho_s(T) e^2}}, \tag{8}$$

where m^* is the effective mass of the charge carriers (Cooper pairs) and e is the elementary charge. This inverse square root relationship ($\lambda_L(T) \propto 1/\sqrt{\rho_s(T)}$) means that experimental measurements of $\lambda_L(T)$, often performed using techniques like muon spin rotation (μSR) or microwave cavity perturbation, provide a direct experimental probe of the superfluid density $\rho_s(T)$, as described by equation (6) in the two-band context.

Complementary to the penetration depth, the superconducting coherence length $\xi(T)$, is the characteristic spatial scale over which the superconducting order parameter can vary significantly, for instance, near defects or boundaries. Physically, it provides an estimate of the average size of a Cooper pair, which can be written as:

$$\xi(T) = \frac{\hbar}{\sqrt{2m^* \Delta_{eff}(T)}}, \tag{9}$$

where $\hbar$ is the reduced Planck constant, and $\Delta_{eff}(T)$ represents an effective superconducting gap parameter that sets the energy scale for coherence. In our two-band model, this effective macroscopic coherence length $\xi(T)$ (which enters the definition of $\kappa(T)$) emerges from the underlying microscopic gaps $\Delta_1(T)$ and $\Delta_2(T)$. While one could conceptually define band-specific coherence lengths $\xi_1(T)$ and $\xi_2(T)$ using $\Delta_1(T)$ and $\Delta_2(T)$ respectively *via* equation (9), the measurable, macroscopic $\xi(T)$ is a composite quantity reflecting the coupled two-band system. Consequently, the overall electromagnetic response and vortex properties, characterized by the macroscopic parameters $\lambda_L(T)$, $\xi(T)$, and $\kappa(T)$, are determined by the microscopic two-band structure.

Crucially, the self-consistent solution of the coupled gap equations (2) yields the temperature dependencies of the individual gaps, $\Delta_1(T)$ and $\Delta_2(T)$. These microscopic gap functions, in turn, dictate the temperature evolution of the macroscopic measurable quantities: the superfluid density $\rho_s(T)$ (*via* equation (6)), the London penetration depth $\lambda_L(T)$ (*via* equation (8), using $\rho_s(T)$ from equation (6)), and the lower critical field $H_{c1}(T)$ (*via* equation (7), using $\lambda_L(T)$ and an appropriately defined composite $\kappa(T)$). Therefore, comparing these theoretically derived temperature dependencies for $\rho_s(T)$, $\lambda_L(T)$, and $H_{c1}(T)$ with experimental data serves as a critical test for the validity of the self-consistent two-band model and allows for the extraction of the underlying intraband and interband coupling parameters (λ_{ij}).

3. RESULTS AND DISCUSSION

In theoretical calculations for the superconductor $SmFeAsO_{0.8}F_{0.2}$, the following parameter values were used: T_c = 44 K; $w_\rho = 0.67$, $\lambda_{11} = 1.23$; $\lambda_{12} = \lambda_{21} = 0.48$; $\lambda_{22} = 0.38$. The fact that both gaps close at T_c indicates the presence of interband coupling in the superconductor $SmFeAsO_{0.8}F_{0.2}$.

Figure 1(a) shows that at low temperatures, Δ_1 and Δ_2 have significant values, and as the temperature increases, both quantities decrease and become zero at T_c. At low temperatures, Δ_1 has a larger value compared to Δ_2. Figure 1(b) presents $\Delta_1(T)$ and $\Delta_2(T)$ normalized by their zero-temperature values, $\Delta_1(0)$ and $\Delta_2(0)$. The temperature dependence of these normalized values has a similar shape, differing only in magnitude, and Δ_1 decreases faster. This behavior indicates characteristic features of superconductivity in the $SmFeAsO_{0.8}F_{0.2}$ superconductor. These plots demonstrate the main features of a multi-gap superconductor, where two gaps exist below T_c, describe the behavior of the energy gaps, and help understand the relationship between the temperature evolution and the characteristics of each gap within the model.

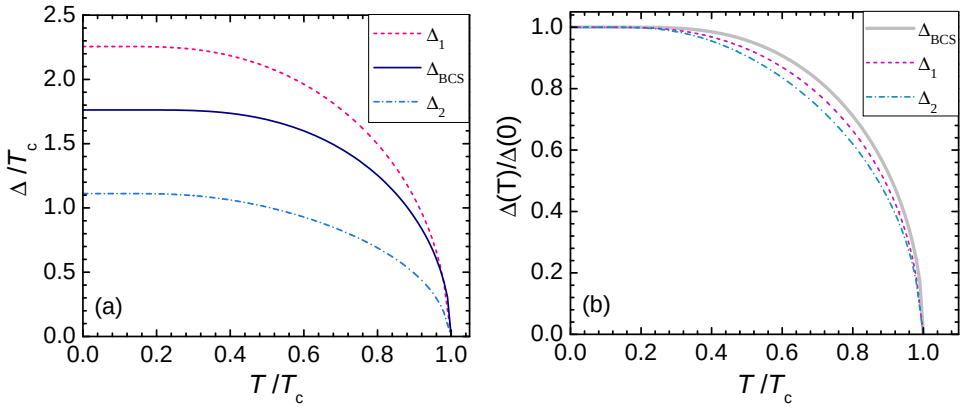

Fig. 1 – (a) Temperature dependence of the two superconducting gaps, Δ_1 and Δ_2, as a function of the reduced temperature T/T_c. (b) Temperature dependence of the gaps normalized to their values at T = 0 K, $\Delta_1(T)/\Delta_1(0)$ and $\Delta_2(T)/\Delta_2(0)$. Parameters are for $SmFeAsO_{0.8}F_{0.2}$.

Figure 2 demonstrates the temperature dependence of the energy gaps Δ_1 and Δ_2 in the superconductor $SmFeAsO_{0.8}F_{0.2}$. Above the critical temperature T_c, the energy gaps vanish, signaling the transition to the normal conducting state. At low temperature, Δ_1 has an initial magnitude exceeding 8.56 meV, while Δ_2 is approximately 4.22 meV. This difference indicates that charge carriers in different bands are characterized by different gaps.

As temperature increases, a smooth decrease in both gaps (Δ_1 and Δ_2) is observed, meaning the superconductivity weakens. However, they decrease at different

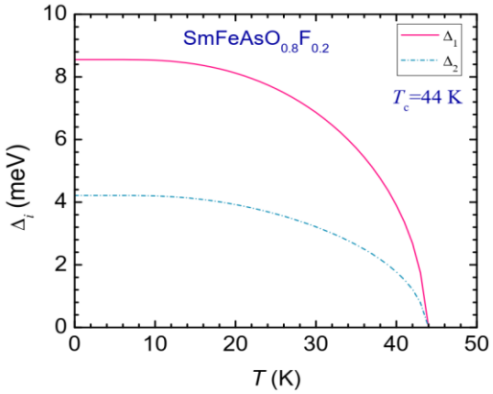

Fig. 2 – Dependence of the energy gaps on temperature in $SmFeAsO_{0.8}F_{0.2}$.

rates, demonstrating the characteristic two-band nature of these superconductors. It is important to note that Δ_1 is more sensitive to temperature changes, while the decrease in Δ_2 becomes steeper near T_c. Consequently, both gap values become zero at the same critical temperature T_c = 44 K. Upon reaching $T = T_c$, both gaps completely disappear, and the material transitions from the superconducting to the normal state.

Figure 3 shows the normalized superfluid density $\rho_s(T)/\rho_s(0)$ as a function of normalized temperature T/T_c for $SmFeAsO_{0.8}F_{0.2}$. It presents the different components of the superfluid density behavior arising within this model. The solid curve (ρ_{tot}) represents the total superfluid density. This curve demonstrates the combined influence of both gaps (*via* ρ_1 and ρ_2 components) on the total density. It is obtained by summing the contributions from the gaps within the model.

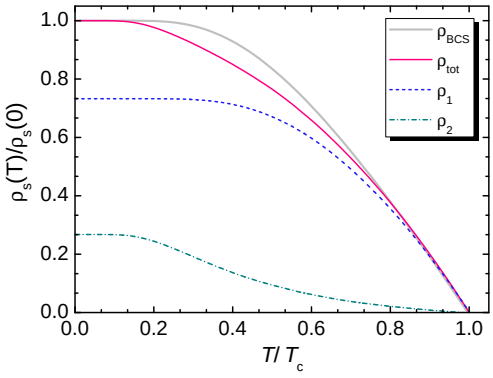

Fig. 3 – Temperature dependence of the normalized superfluid density $\rho_s(T)/\rho_s(0)$.

The dashed (for ρ_1) and dash-dotted (for ρ_2) curves represent the contributions of the individual gaps to the total density. ρ_1 has a shallower slope and a larger value

at low temperatures, and it begins to decrease later compared to ρ_2. The curve for ρ_2 shows corresponding behavior, reflecting a steeper and more rapid decrease. This indicates that the contribution of each gap has distinct characteristics in its temperature dynamics, and both contributions are significant. Additionally, there is a curve for ρ_{BCS}, which displays the behavior of standard BCS superconductivity, characterized by a single-gap contribution.

Overall, Fig. 3 demonstrates the contribution of each gap to the total superfluidity, highlighting the multi-gap structure and showing a significant difference from standard single-gap superconductivity. Clearly, multiple types of charge carriers exist, manifesting through multiple gaps in the material $SmFeAsO_{0.8}F_{0.2}$.

Figure 4 illustrates the key role of the two-gap model in describing the superconductivity of $SmFeAsO_{0.8}F_{0.2}$. It displays the temperature dependence of the normalized superfluid density $(\rho_s(T)/\rho_s(0))$, calculated *via* the ratio $\lambda^2(0)/\lambda^2(T)$ (where λ is the magnetic penetration depth), obtained from penetration depth measurements [31]. The experimental data, marked by points on the graph, clearly demonstrate that the simple single-gap BCS model (dashed curve) fails to accurately describe the observed temperature dependence.

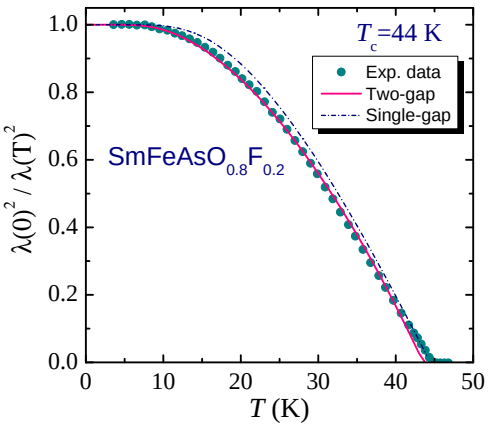

Fig. 4 – Comparison of theoretical predictions for the temperature-dependent normalized superfluid density $\rho_s(T)/\rho_s(0)$, with experimental data obtained from $SmFeAsO_{0.8}F_{0.2}$ superconductor. The solid and dash-dotted lines represent theoretical calculations based on the two-band model and the single-band BCS model, respectively. Experimental data from Carrington [31] are represented by circle symbols.

Single-gap BCS model does not reproduce the experimental saturation of the superfluid density at low temperatures and decreases too rapidly near T_c, failing to match the shape of the experimental curve.

In contrast, the two-gap model (solid line), which considers two different energy gaps, shows excellent agreement with the experimental data. This indicates that

superconductivity in $SmFeAsO_{0.8}F_{0.2}$ is governed by at least two types of carrier pairing, possessing different energy gap magnitudes, and such multi-gap behavior plays a crucial role. Such behavior is indicative of s^{++} superconductivity, a characteristic feature of which is the saturation of the superconducting carrier density at low temperatures, and supports the applicability of two-band theory to iron-pnictide based materials.

The difference in the curves indicates that a single-gap BCS mechanism cannot fully describe the system, emphasizing the importance of a more complex, multi-gap pairing mechanism in these superconductors, both for $SmFeAsO_{0.8}F_{0.2}$ and other similar compounds of the FeSC family. The good agreement between the data and calculations based on the two-gap model confirms that this mechanism is dominant in this case and is more adequate compared to simple BCS models for describing the superconducting phase in this material and other Fe-containing superconductors. This shows that the observed superconducting behavior in $SmFeAsO_{0.8}F_{0.2}$ stems from the complex multi-band structure of its electronic states.

To further evaluate the applicability and robustness of the self-consistent two-gap model, we extend our analysis to another prominent iron-based superconductor, LiFeAs, known for its multi-gap characteristics. For the theoretical calculations within the two-gap model applied to LiFeAs, the following parameter set was utilized, chosen to best reproduce the experimental findings: a critical temperature T_c = 17.5 K (matching the experimental value for the sample used in [8]), an effective mass $m^* = 2.5m_e$, a band weighting factor $w_\rho = 0.65$ for the superfluid density (equation (6)), and intra- and interband coupling constants $\lambda_{11} = 1.38$, $\lambda_{12} = \lambda_{21} = 0.33$, and $\lambda_{22} = 0.43$ (used in (2) and (4)). Figures 5 and 6 present a direct comparison between theoretical predictions derived using these parameters within our framework and the single-band BCS model, alongside experimental data for LiFeAs.

Figure 5 illustrates the temperature evolution of the normalized superfluid density, $\rho_s(T)/\rho_s(0)$. The experimental data points, represented by circle symbols, are derived from penetration depth measurements reported by Song *et al.* [8]. The inadequacy of the single-band BCS model (solid gray line) is immediately striking. It predicts a significantly faster suppression of ρ_s below T_c than observed and completely fails to capture the distinct flattening, or saturation, of the superfluid density at low temperatures. This low-temperature saturation is a crucial experimental feature, physically signifying the opening of a full, nodeless superconducting gap, which inhibits low-energy quasiparticle excitations as $T \to 0$.

In compelling contrast, the solid blue line, depicting the total $\rho_s(T)/\rho_s(0)$ calculated using our self-consistent two-gap approach, accurately traces the experimental data across the entire superconducting temperature range. It naturally reproduces the essential low-temperature saturation and the precise curvature near T_c. This finding resonates strongly with the analysis by Song *et al.* [8] themselves, who concluded that

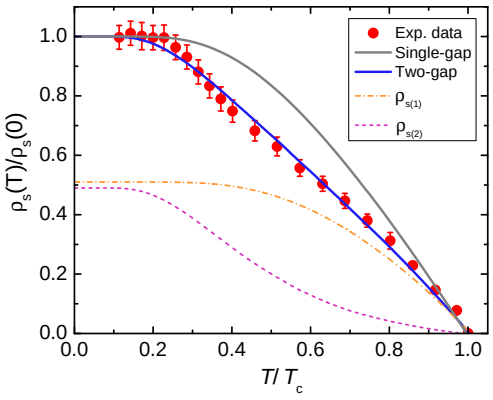

Fig. 5 – Comparison of theoretical predictions for the temperature-dependent normalized superfluid density $\rho_s(T)/\rho_s(0)$, with experimental data obtained from LiFeAs superconductor. The solid, dash-dotted, and dashed lines represent theoretical calculations based on two-gap model, respectively. The solid gray curve shows the results of the single-band BCS model calculation. The circle symbols represent experimental data from Song *et al.* [8].

a two-gap model was indispensable for fitting their $\lambda_L(T)$ measurements accurately. They observed a low-temperature behavior in penetration depth variation ($\Delta\lambda \sim T^n$ with $n > 3.5$) consistent with nodeless gaps, possibly of $s^{\pm}$ symmetry, in the presence of weak scattering. Our self-consistent calculation provides a strong theoretical underpinning for these observations. By incorporating two distinct, coupled gaps arising from different electronic bands (whose individual contributions $\rho_{s(1)}$ and $\rho_{s(2)}$ are shown by the dash-dotted and dashed lines), our model intrinsically yields the behavior consistent with these experimental findings, highlighting the physical origin of the deviation from simple BCS theory.

Complementary insights are gleaned from Fig. 6, which presents the temperature dependence of the London penetration depth, $\lambda_L(T)$. Recalling that $\lambda_L(T)$ is inversely proportional to the square root of the superfluid density ($\lambda_L(T) \propto [\rho_s(T)]^{-1/2}$), this plot provides a different but physically equivalent view of the behavior of a superconducting condensate. The circle symbols again denote the experimental data from Song *et al.* [8]. The single-band BCS prediction (solid gray line) shows $\lambda_L(T)$ increasing far too steeply with temperature, markedly disagreeing with the experimental observation of a very weak temperature dependence at low T. This weak dependence is the direct manifestation of the superfluid density saturation seen in Fig. 5. Our two-gap model (solid blue line), however, aligns remarkably well with the experimental data points. It successfully captures the quasi-temperature-independent behavior of λ_L at low temperatures – the expected signature of a fully gapped superconductor, consistent with the interpretation of Song *et al.* [8] - and accurately describes the subsequent rise as $T \to T_c$.

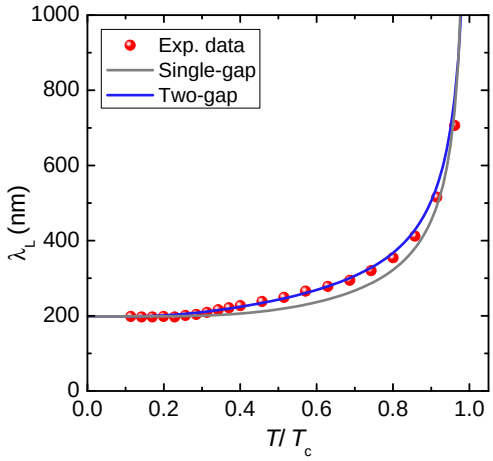

Fig. 6 – Temperature dependence of the London penetration depth λ_L in LiFeAs superconductor. The solid blue (gray) lines represent theoretical calculations based on two-gap (single-band BCS) models, respectively. The circle symbols represent experimental data from Song *et al.* [8].

Taken together, the excellent agreement demonstrated in Figs. 5 and 6 between our self-consistent two-gap calculations and the detailed experimental results from Song *et al.* [8] provides robust validation for our theoretical framework. It underscores that the superconducting phenomenology of LiFeAs is intrinsically tied to its multi-band electronic structure, necessitating a multi-gap description. The clear failure of the single-band model serves to emphasize this point. Our results offer a physically grounded, theoretical confirmation of the multi-gap, nodeless superconductivity inferred from experiments in LiFeAs, reinforcing the importance of considering multi-band physics for understanding iron-based superconductors.

Figure 7 presents the theoretical results for $SmFeAsO_{0.9}F_{0.1}$ obtained using the self-consistent two-band model with parameters chosen to represent this compound ($T_c = 53$ K, $m^* = 3m_e$, w_ρ = 0.584, $\lambda_{11} = 1.64$, $\lambda_{12} = \lambda_{21} = 0.52$, $\lambda_{22} = 0.4$). It encapsulates the core features arising from multi-gap superconductivity in this system.

Panel 7(a) reveals the distinct temperature evolution of the two superconducting gaps, $\Delta_1(T)$ and $\Delta_2(T)$, calculated self-consistently *via* equation (2). The substantial difference in their zero-temperature values, with Δ_1 being significantly larger than Δ_2, stems directly from the disparity in intraband coupling strengths ($\lambda_{11} = 1.64 >> \lambda_{22} = 0.4$). This reflects stronger intrinsic Cooper pairing within Band 1, likely associated with specific Fermi surface sheets (*e.g.* hole pockets often implicated in stronger pairing tendencies in pnictides), compared to the weaker pairing interactions within Band 2. Despite these differences, both gaps vanish simultaneously at the single experimental $T_c = 53$ K. This synchronization is a crucial consequence of the finite interband coupling ($\lambda_{12} = \lambda_{21} = 0.52$), which mediates pair scattering between

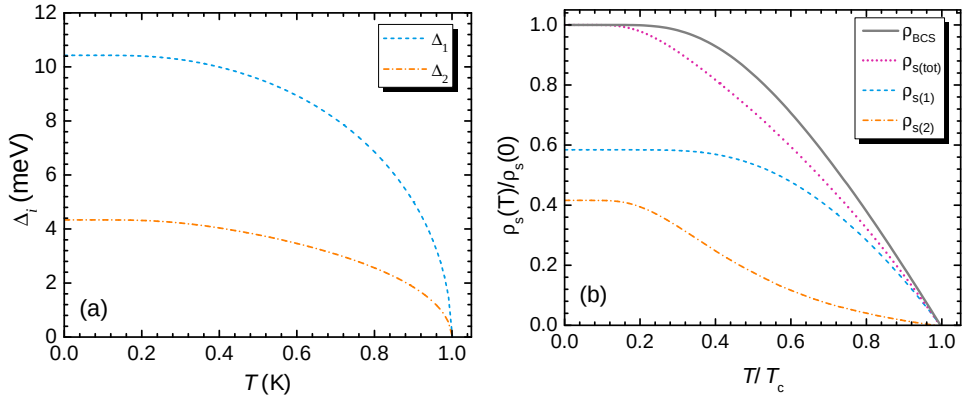

Fig. 7 – (a) Temperature dependence of the two superconducting gaps, Δ_1 and Δ_2, as a function of the reduced temperature T/T_c. (b) Temperature dependence of the normalized superfluid density $\rho_s(T)/\rho_s(0)$. Parameters are for $SmFeAsO_{0.9}F_{0.1}$.

the bands and enforces a common transition temperature, consistent with experimental observations and dictated by the largest eigenvalue of the coupling matrix (equation 3). The interplay between the strong λ_{11} driving Δ_1 towards a more standard BCS-like curvature, and the interband coupling λ_{12} influencing and partially stabilizing the smaller Δ_2, leads to their distinct temperature profiles below T_c. The effective mass ($m^* = 3m_e$), indicating moderate electron correlations compared to free electrons, primarily sets the absolute scale for derived quantities like penetration depth but does not alter the normalized temperature dependencies shown.

Panel 7(b) illustrates the macroscopic consequence of this two-gap structure on the normalized superfluid density, $\rho_s(T)/\rho_s(0)$. The total superfluid density ($\rho_{s(tot)}$, dotted pink line), calculated as a weighted sum of the individual band contributions *via* equation (6) with weighting factor $w_\rho = 0.584$, stands in stark contrast to the prediction of a simple single-band BCS model (thick gray line). The w_ρ value indicates that Band 1, with the larger gap, contributes approximately 58.4% to the total zero-temperature superfluid density ($\rho_{s1}(0)/\rho_s(0)$), consistent with its stronger pairing interaction ($\lambda_{11} >> \lambda_{22}$), while Band 2 contributes the remaining $\sim$41.6%.

Most importantly, the two-band calculation accurately captures the pronounced saturation (very weak temperature dependence) of ρ_s at low temperatures ($T << T_c$). This flatness is the *hallmark experimental signature* of a fully gapped superconductor. Physically, it arises because both Δ_1 and Δ_2 remain finite across their respective Fermi surface sections, providing a *robust energy barrier* that exponentially suppresses the thermal excitation of quasiparticles as $T \to 0$. This maintains a nearly constant condensate density. The single-band BCS model, lacking this multi-gap complexity, predicts a much steeper decrease in ρ_s below T_c and fails to reproduce

the experimentally observed saturation.

Examining the individual band contributions provides further insight: ρ_{s1} (dash-dotted blue line) exhibits very strong saturation due to the large, robust gap Δ_1. In contrast, ρ_{s2} (dashed line) shows a more noticeable decrease at lower temperatures because the smaller gap Δ_2 allows for easier quasiparticle excitation as thermal energy k_BT becomes comparable. The overall shape of $\rho_{s(tot)}(T)$ is therefore a non-trivial superposition, weighted by w_ρ, reflecting the coexistence of two distinct gap scales and their different temperature dependencies governed by the full set of coupling constants (λ_{ij}). This analysis underscores the necessity of the two-band model to describe the superfluid response in multi-band systems like $SmFeAsO_{0.9}F_{0.1}$, accurately linking the microscopic pairing interactions to macroscopic observable properties.

Figure 8 provides a physically equivalent perspective by plotting the calculated temperature dependence of the London penetration depth, $\lambda_L(T)$, derived from the total superfluid density using the relation $\lambda_L(T) = [\mu_0\rho_s(T)e^2/m^*]^{-1/2} \propto [\rho_s(T)]^{-1/2}$. This parameter is a key experimental observable. Consistent with the $\rho_s(T)$ behavior, the calculated total $\lambda_L(T)$ (solid line) demonstrates pronounced flatness at low temperatures before rising steeply near $T_c = 53$ K. This low-temperature quasi-independence

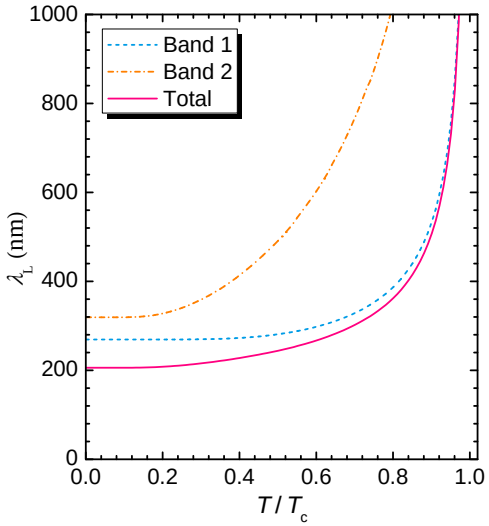

Fig. 8 – Temperature dependence of the normalized superfluid density $\rho_s(T)/\rho_s(0)$. Parameters are for $SmFeAsO_{0.9}F_{0.1}$.

of λ_L is the hallmark experimental signature of fully gapped, nodeless superconductivity, frequently observed in materials like $SmFeAsO_{1-x}F_x$ near optimal doping. The figure conceptually illustrates how this arises from the band contributions: Band 1

(dashed line, derived from $1/\sqrt{\rho_{s1}}$ scaled) yields a small, very flat contribution due to the robust large gap Δ_1. Band 2 (dash-dotted line, from $1/\sqrt{\rho_{s2}}$ scaled) yields a larger, more temperature-sensitive contribution due to the smaller Δ_2 allowing easier thermal excitation. The measured total λ_L is a combination ($\lambda_L^{-2} \propto \rho_{s1} + \rho_{s2}$), where the strong condensate in Band 1 dictates the small absolute value and flatness at low T, while thermal effects in Band 2 primarily govern the initial rise as temperature increases. The ability of the self-consistent two-band model, using this specific, physically reasonable set of parameters ($\lambda_{ij}, w_\rho, m^*, T_c$), to reproduce these characteristic low-temperature saturation features in both ρ_s and λ_L provides compelling theoretical support for its validity in describing the complex multi-band superconductivity of $SmFeAsO_{0.9}F_{0.1}$ and related iron pnictides.

We further validate our model by analyzing the lower critical magnetic field, $H_{c1}(T)$. This field represents the thermodynamic threshold at which it becomes energetically favorable for magnetic flux vortices to penetrate a type-II superconductor. Fundamentally, H_{c1} is determined by the balance between the energy cost of maintaining shielding currents and the magnetic energy gained by flux entry. In the Ginzburg-Landau framework, this leads to $H_{c1} \propto (\ln \kappa)/\lambda_L^2$, where λ_L is the magnetic penetration depth and $\kappa = \lambda_L/\xi$ is the Ginzburg-Landau parameter involving the coherence length ξ. Since the superfluid density $\rho_s \propto 1/\lambda_L^2$, $H_{c1}(T)$ serves as a sensitive thermodynamic probe of $\rho_s(T)$ and the underlying superconducting gap structure.

Figure 9 directly compares experimental $H_{c1}(T)$ data for $SmFeAsO_{0.9}F_{0.1}$ (circles) [32] with theoretical predictions, normalized to their zero-temperature values. The experimental data show a characteristic flattening at low temperatures followed by a smooth decrease towards T_c. Evaluating the theoretical models highlights the inadequacy of a standard single-band BCS description (dot-dashed line). This simple model fails to capture the observed temperature dependence, particularly predicting a much steeper decrease than seen experimentally.

In stark contrast, the prediction from our self-consistent two-band model (solid blue line) shows excellent agreement with the experimental data across the entire temperature range. Crucially, this calculation uses the *identical* set of parameters (yielding the temperature-dependent gaps $\Delta_1(T)$ and $\Delta_2(T)$) previously determined from fitting the superfluid density and penetration depth behavior shown in Figs. 7b and 8. Our model accurately reproduces both the low-temperature saturation, characteristic of a fully gapped state, and the overall curve shape up to T_c.

This agreement across different physical quantities provides strong validation for the two-band approach. It demonstrates that the thermodynamic stability against magnetic field penetration (H_{c1}) is directly governed by the same two-gap electronic structure that determines the superfluid response (ρ_s, λ_L). The success underscores that our model correctly captures how the temperature evolution of the Cooper pair

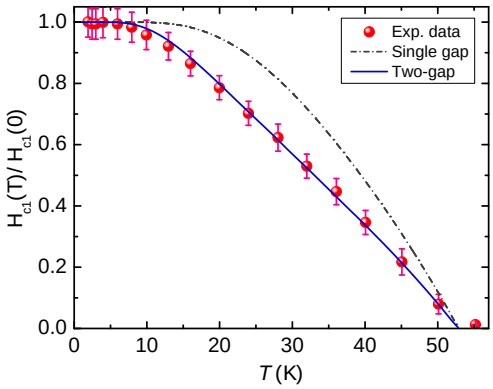

Fig. 9 – Comparison of theoretical predictions (solid line) for the temperature-dependent normalized lower critical magnetic field $H_{c1}(T)/H_{c1}(0)$, with experimental data obtained from $SmFeAsO_{0.9}F_{0.1}$ superconductor. The circle symbols represent experimental data [32].

condensate, described by the coupled gaps, dictates the macroscopic magnetic properties. Conversely, the failure of the single-band model emphasizes that neglecting the multi-band nature leads to a fundamentally incorrect description of how the superconductor resists magnetic flux entry. Therefore, the $H_{c1}(T)$ analysis provides robust, independent thermodynamic evidence confirming the necessity of the self-consistent two-band framework for understanding $SmFeAsO_{0.9}F_{0.1}$.

4. CONCLUSION

In this work, we have presented a comprehensive theoretical investigation into the superfluid response of iron-based superconductors (FeSCs), utilizing a self-consistent two-band model. This approach is necessitated by the intrinsic multi-band electronic structure characteristic of these materials, which commonly leads to the opening of multiple superconducting energy gaps on different Fermi surface sheets. We have calculated the temperature dependencies of key superconducting parameters – the superfluid density (ρ_s), the London penetration depth (λ_L), and the lower critical magnetic field (H_{c1}) – for representative FeSCs, namely $SmFeAsO_{1-x}F_x$ and LiFeAs.

Our comparative analysis clearly demonstrates the limitations of the standard single-gap BCS framework in describing the experimental observations in these materials. The single-gap model fails to reproduce crucial features, particularly the saturation of ρ_s (and λ_L) at low temperatures characteristic of fully gapped superconductors, and it inadequately describes the overall temperature dependence of ρ_s, λ_L, and H_{c1}. In contrast, the self-consistent two-band model provides a significantly improved and, in many cases, quantitatively accurate description of the experimental data across the full temperature range below T_c.

The success of the two-band model stems from its explicit incorporation of two distinct superconducting gaps (Δ_1 and Δ_2) and their respective coupling constants (λ_{ij}). We showed that these gaps exhibit unique temperature dependencies, governed by both intraband pairing strengths and crucial interband coupling, the latter being responsible for the emergence of a single transition temperature T_c. The total superfluid response (ρ_s, λ_L, H_{c1}) arises as a non-trivial superposition of the contributions from these two distinct electronic bands, accurately capturing the experimentally observed behavior. This theoretical framework successfully models the macroscopic consequences of Cooper pairing occurring across multiple electronic bands.

The fairly good agreement achieved between our theoretical calculations and diverse experimental data ($\rho_s(T)$ from $\lambda_L^{-2}(T)$ measurements, $\lambda_L(T)$ directly, and $H_{c1}(T)$) for different FeSC compounds validates the applicability of the self-consistent two-band approach. It underscores the fundamental importance of multi-band physics in determining the superconducting properties of these complex materials. The results presented here provide a robust theoretical basis for interpreting experimental findings in FeSCs, highlight the distinct signatures of multi-gap superconductivity in their superfluid response, and contribute to the broader effort to understand the intricacies of unconventional superconductivity in iron pnictides and related systems.

Acknowledgements. O.K.G. expresses his gratitude to the Academy of Sciences of Uzbekistan for financial support.

REFERENCES

1. Y. Kamihara, T. Watanabe, M. Hirano, and H. Hosono, Journal of the American Chemical Society **130**, 3296 (2008).
2. J. Bardeen, L. N. Cooper, and J. R. Schrieffer, Phys. Rev. **108**, 1175 (1957).
3. G. R. Stewart, Rev. Mod. Phys. **83**, 1589 (2011).
4. M. Tinkham, *Introduction to superconductivity* (2nd edn., Courier Corporation, 1996).
5. A. Amato, R. Khasanov, H. Luetkens, and H.-H. Klauss, Physica C **469**, 606 (2009).
6. P. Materne, S. Kamusella, R. Sarkar, T. Goltz, J. Spehling, H. Maeter, L. Harnagea, S. Wurmehl, B. Büchner, H. Luetkens, C. Timm, and H.-H. Klauss, Phys. Rev. B **92**, 134511 (2015).
7. C. Ren, Z. Wang, H. Luo, H. Yang, L. Shan, and H. Wen, Physica C **469**, 599 (2009).
8. Y. J. Song, J. S. Ghim, J. H. Yoon, K. J. Lee, M. H. Jung, H.-S. Ji, J. H. Shim, Y. Bang, and Y. S. Kwon, Europhysics Letters **94**, 57008 (2011).
9. M. Abdel-Hafiez, P. J. Pereira, S. A. Kuzmichev, T. E. Kuzmicheva, V. M. Pudalov, L. Harnagea, A. A. Kordyuk, A. V. Silhanek, V. V. Moshchalkov, B. Shen, H.-H. Wen, A. N. Vasiliev, and X.-J. Chen, Phys. Rev. B **90**, 054524 (2014).
10. D. V. Evtushinsky, V. B. Zabolotnyy, L. Harnagea, A. N. Yaresko, S. Thirupathaiah, A. A. Kordyuk, J. Maletz, S. Aswartham, S. Wurmehl, E. Rienks, R. Follath, B. Büchner, and S. V. Borisenko, Phys. Rev. B **87**, 094501 (2013).
11. K. Hashimoto, T. Shibauchi, S. Kasahara, K. Ikada, S. Tonegawa, and Y. Matsuda, Phys. Rev. Lett. **102**, 027002 (2009).

12. P. J. Hirschfeld, M. M. Korshunov, and I. I. Mazin, Rep. Prog. Phys. **74**, 124508 (2011).
13. A. Carrington and F. Manzano, Physica C **385**, 205 (2003).
14. H. Ding, P. Richard, K. Nakayama, K. Sugawara, T. Arakane, Y. Sekiba, A. Takayama, S. Souma, T. Sato, and T. Takahashi, EPL **83**, 47001 (2008).
15. Y. Nakai, T. Iye, S. Kitagawa, K. Ishida, S. Ikeda, S. Yoshizawa, M. Hirano, and H. Hosono, Phys. Rev. B **81**, 100505R (2008).
16. V. G. Kogan, C. Martin, and R. Prozorov, Phys. Rev. B **80**, 014507 (2009).
17. H. Padamsee, J. E. Neighbor, and C. A. Shiffman, J. Low. Temp. Phys. **12**, 387 (1973).
18. R. Prozorov and V. G. Kogan, Rep. Prog. Phys. **74**, 124505 (2011).
19. R. Khasanov, M. Bendele, A. Amato, K. Conder, H. Keller, H.-H. Klauss, H. Luetkens, and E. Pomjakushina, Phys. Rev. Lett. **104**, 087004 (2010).
20. H. Kim, R. T. Gordon, M. A. Tanatar, J. Hua, U. Welp, W. K. Kwok, N. Ni, S. L. Bud'ko, P. C. Canfield, A. B. Vorontsov, and R. Prozorov, Phys. Rev. B **82**, 060518 (2010).
21. K. Hashimoto, S. Kasahara, R. Katsumata, Y. Mizukami, M. Yamashita, H. Ikeda, T. Terashima, A. Carrington, Y. Matsuda, and T. Shibauchi, Phys. Rev. Lett. **108**, 047003 (2012).
22. K. Cho, M. A. Tanatar, N. Spyrison, H. Kim, Y. Song, P. Dai, C. L. Zhang, and R. Prozorov, Phys. Rev. B **86**, 020508 (2012).
23. A. Bussmann-Holder, R. Micnas, and A. R. Bishop, EPJ B **37**, 345 (2004).
24. V. G. Kogan, C. Martin, and R. Prozorov, Phys. Rev. B **80**, 014507 (2009).
25. A. Bussmann-Holder, arXiv:0909.3603 (2009).
26. R. M. Fernandes and J. Schmalian, Phys. Rev. B **82**, 014521 (2010).
27. V. G. Kogan and R. Prozorov, Phys. Rev. B **93**, 224515 (2016).
28. H. Suhl, B. T. Matthias, and L. R. Walker, Phys. Rev. Lett. **3**, 552 (1959).
29. V. A. Moskalenko, Phys. Met. Metallogr. **8**, 25 (1959).
30. B. T. Geilikman, R. O. Zaitsev, and V. Z. Kresin, Sov. Phys. Solid State **9**, 642 (1967).
31. A. Carrington, Comptes Rendus. Physique **12**, 502 (2011).
32. Z.-S. Wang, *The superconducting properties research of iron based-122 by transport and scanning micro-squid measurements*, PhD Theses, Université de Grenoble; University of Chinese Academy of Sciences (2012).